

# Identification and Analysis of Multiple Factors Controlling Solar-driven H<sub>2</sub>O<sub>2</sub> Synthesis Using Engineered Polymeric Carbon Nitride

Yubao Zhao (✉ [ybzhao@gzhu.edu.cn](mailto:ybzhao@gzhu.edu.cn))

Guangzhou University <https://orcid.org/0000-0001-7982-1116>

Jingyu Gao

Guangzhou University

Lina Li

Guangzhou University

Sheng Chen

Nanjing University of Science and Technology <https://orcid.org/0000-0002-6224-2051>

Chun Hu

Guangzhou University

Wonyong Choi

Pohang University of Science and Technology <https://orcid.org/0000-0003-1801-9386>

---

## Article

**Keywords:** Photocatalysis, Reaction Mechanism, Hydrogen Peroxide, Flow Photo-reaction, Photoinduced charge transfer mechanism

**Posted Date:** September 21st, 2020

**DOI:** <https://doi.org/10.21203/rs.3.rs-74522/v1>

**License:**  This work is licensed under a Creative Commons Attribution 4.0 International License.

[Read Full License](#)

---

**Version of Record:** A version of this preprint was published at Nature Communications on June 17th, 2021. See the published version at <https://doi.org/10.1038/s41467-021-24048-1>.

# Abstract

Solar-driven hydrogen peroxide ( $\text{H}_2\text{O}_2$ ) production presents unique merits of sustainability and environmental friendliness. Herein, highly efficient solar-driven  $\text{H}_2\text{O}_2$  production through dioxygen reduction is achieved by employing polymeric carbon nitride (PCN) framework with sodium cyanamate moiety (PCN-NaCA), affording a superior  $\text{H}_2\text{O}_2$  production rate of  $175 \mu\text{mol/h}$  on  $10 \text{ mg}$  photocatalyst and a notable apparent quantum yield of  $27.6\%$  at  $380 \text{ nm}$ . The overall photocatalytic transformation process is systematically analyzed using various steady-state/transient spectroscopic and computational methods. The presence of sodium cyanamate moiety in PCN-NaCA induces the following multiple effects: enhancing photon absorption, creating the coexistence of p-type and n-type domains, strengthening surface adsorption of dioxygen, and favoring highly selective  $2\text{e}^-$  ORR. In particular, the adsorption of dioxygen on PCN-NaCA enhances the population and lifetime of trapped electrons in the ps-ns time regime, which should have a notable synergic effect on oxygen reduction process.

## Introduction

Hydrogen peroxide ( $\text{H}_2\text{O}_2$ ) is a versatile chemical, functioning as a green oxidant and a clean liquid fuel. In this context, photochemical  $\text{H}_2\text{O}_2$  production is attracting great interests as an alternative solar fuel option.<sup>1</sup> Solar-driven  $\text{H}_2\text{O}_2$  synthesis presents unique features of remarkable sustainability and environmental friendliness as compared to the traditional anthraquinone process and direct synthesis method.<sup>2</sup> However, the solar conversion efficiency bottleneck is the major obstacle to the goal of sustainable  $\text{H}_2\text{O}_2$  production.

A plethora of photocatalysts have thus been developed to improve the solar-driven  $\text{H}_2\text{O}_2$  production efficiency. Among various photocatalysts, polymeric carbon nitride (PCN) consisting of the organic framework has the advantage of easy structural optimization;<sup>3</sup> its surface dangling functional groups and the conjugated electronic structure can be facilely modified for efficient catalytic reactions. This unique advantage can be maximized only if the structure-photocatalytic activity relationship is clearly understood and taken into account in designing the PCN structure and composition.<sup>4</sup> However, understanding the overall photocatalytic process is challenging since it involves multiple consecutive steps, which include photon absorption/excitation, emissive decay, photo-induced charge trapping/separation, charge transport to the surface-active-sites, interfacial charge transfer with the surface adsorbed reactants, intermediates conversions, and finally product desorption (Fig. 1). Each step in the complicated process contributes to the overall solar conversion efficiency.<sup>5</sup>

The pendant amino group on PCN is proven to introduce energetically deeper trapping sites which may negatively influence the photocatalytic activity.<sup>29</sup> Various methods for modifying the structure and composition of PCN have been investigated to improve its photocatalytic activity.<sup>6</sup> For example, substitution of the pendant amino groups by cyanamide units improves the solar hydrogen evolution

reaction (HER) activity of the PCN photocatalysts.<sup>26,27</sup> However, a comprehensive mechanistic understanding on how the specific structural features influence each step in the photocatalytic  $2e^-$  oxygen reduction reaction (ORR) is challenging and relatively unexplored while such information is critical for the rational design of a highly efficient solar-driven  $H_2O_2$  production system. Herein, superior solar-driven  $2e^-$  ORR performance is achieved on an engineered PCN framework. The key mechanistic features of the overall photocatalytic process are analyzed by tracing the consecutive electrons transfer steps involved in the photoinduced processes and the subsequent surface reactions (Fig. 1). Introduction of sodium cyanamate moiety creates the coexistence of p-type and n-type domains in the framework. It exhibits enhanced photon absorption capacity and retarded emissive charge-recombination by trapping a significant fraction of charge carriers. It also shows enhanced accumulation of surface charge, stronger surface affinity for dioxygen, and more catalytic active sites for selective  $2e^-$  ORR.

## Results

### Synthesis and performance of the photocatalysts in the photocatalytic $H_2O_2$ production.

PCN was synthesized by condensation reaction of the melamine-cyanuric acid complex under high temperature (Fig. 2a). The resulting PCN was further treated with sodium thiocyanate (NaSCN) molten salt to tailor the conjugated electronic structure and the surface properties. Further condensation reaction occurs in the molten salt and leads to two favorable structural features: (1) improved polymerization degree and expanded conjugated electronic structure; and (2) conversion of the amino group to the sodium cyanamate moiety (Figs. 2a, S1, and S2). The PCN frameworks with sodium cyanamate moiety is denoted by PCN-NaCA- $n$  ( $n$ : 1, 2, and 3 refer to the sample with the salt/PCN weight ratio of 0.5, 1, and 2, respectively). The structure of PCN for the simulation is the linear melon with infinite repeating units. For PCN-NaCA-2, sodium ion interacts with four nitrogen atoms from two adjacent heptazine units in the optimized structure (Figs. 2b).

The photocatalytic selective reduction of  $O_2$  to  $H_2O_2$ , in an ideal scenario, should employ  $H_2O$  as the proton/electron donor, so that there is no additional  $CO_2$  emission from this process. However, the electron and proton extraction through water oxidation process ( $2H_2O \rightarrow 4H^+ + 4e^- + O_2$ ) is inefficient as the hole transfer kinetics toward water oxidation is sluggish, causing severe charge recombination, which results in low solar conversion efficiency. In natural photosynthesis, electrons/protons are extracted from water *via* complicated bio-enzymatic reactions and subsequently used in transforming  $CO_2$  to biomass to achieve the energy-uphill reaction. An alternative solution is to utilize more reactive organic substances (as an electron/proton donor instead of water) that are abundant and cheap. In the rapidly rising biodiesel industry, glycerol is the byproduct and its yield accounts for 10 wt.% of the biodiesel production, but the limited consumption of glycerol makes it surplus. Developing a proper process of consuming and valorizing glycerol well matches the market need. Moreover, glycerol is non-toxic and bio-degradable, rendering it an ideal practical electron/proton donor for the solar fuel production.<sup>38-41</sup> Therefore, solar

production of H<sub>2</sub>O<sub>2</sub> with glycerol as the electron/proton donor can be proposed as an environmentally benign and cost-effective solution.

Figure 3a compares the photoproduction of H<sub>2</sub>O<sub>2</sub> in the presence of glycerol using various PCN samples in 50 mL batch reaction. Pure PCN generates 0.23 mM H<sub>2</sub>O<sub>2</sub> in 45 min irradiation, while PCN-NaCA-*n* samples exhibit markedly enhanced activity for H<sub>2</sub>O<sub>2</sub> production. PCN-NaCA-2 shows the optimum photocatalytic performance, producing 2.80 mM H<sub>2</sub>O<sub>2</sub> in 45 min irradiation. The H<sub>2</sub>O<sub>2</sub> production rate reaches a high value of 173 μmol/h (by 10 mg PCN-NaCA-2) under solar simulator irradiation (Figure S3).<sup>11,12,15-17</sup> Mesoporous carbon nitride (mpg-C<sub>3</sub>N<sub>4</sub>), which is an outstanding photocatalyst for H<sub>2</sub> production, however, shows low performance in the selective 2e<sup>-</sup> ORR with producing only 0.53 mM H<sub>2</sub>O<sub>2</sub>.

As the H<sub>2</sub>O<sub>2</sub> production reaction involves transfer of protons as well as electrons, the acidic media is normally more favorable.<sup>15-17</sup> However, PCN-NaCA-2 favors neutral to mild basic conditions for efficient solar-driven H<sub>2</sub>O<sub>2</sub> production (Figs. 2b, S4). The apparent quantum yield (AQY) of the photoproduction of H<sub>2</sub>O<sub>2</sub> was measured using monochromatic light as a function of wavelength (Fig. 3c). The AQY is 27.6% and 11.8% at 380 nm and 420 nm, respectively, and rapidly decreases with further increasing the wavelength, which matches well with the absorption spectral profile of the photocatalyst. The fact that the action spectrum of H<sub>2</sub>O<sub>2</sub> production is closely correlated with the optical absorption spectrum supports the photocatalytic mechanism based on ORR.

To further explore the performance of PCN-NaCA-2 in large scale reaction, the continuous serial micro-batch reactor, which typically has high surface-area-to-volume ratio and allows for more efficient irradiation of the solid-gas-liquid triphasic reaction system, is employed (Figure S5).<sup>-</sup> As shown in Fig. 3d, the H<sub>2</sub>O<sub>2</sub> production rate increases with PCN-NaCA-2 concentration, and reaches plateau when concentration is higher than 2400 mg/L. With the photocatalyst concentration of 2400 mg/L, H<sub>2</sub>O<sub>2</sub> concentration reaches high values of 12.3 and 18.6 mM with short retention time of 36 min and 72 min, respectively. While for PCN, flow photo-reaction with 36 min retention time only affords 0.5 mM H<sub>2</sub>O<sub>2</sub> under the same reaction conditions. PCN-NaCA-2 shows a superior H<sub>2</sub>O<sub>2</sub> production performance which is 24.6 times of that on PCN.

**Mechanistic investigations on the photons to chemical energy conversion process.** For a comprehensive understanding of the rationale for the above-mentioned superior photoactivity of the cyanamate-modified PCN, we carried out systematic mechanistic investigations on the following aspects: 1) excitation and emissive decay process; 2) non-emissive states, focusing on population and decay kinetics of the trapped electrons; and 3) surface processes that include surface electron trapping, dioxygen adsorption, and ORR activity and selectivity (Fig. 1).

Compared to PCN, the photon absorption spectra of PCN-NaCA-*n* samples show significantly improved absorbance at 350 nm – 380 nm which is commonly observed in the conjugated aromatic systems with π – π\* transition (Fig. 4a).<sup>·</sup> The absorbance at 450–500 nm is attributed to n – π\* transitions involving

lone pair electrons on the N atoms of the amino group and the secondary amine unit in the framework. The  $n - \pi^*$  transition is forbidden for perfectly symmetric and planar s-triazine/heptazine units, but they become allowed as the structures develop distortions.<sup>51,52</sup> For the PCN-NaCA-*n* samples, the improved polymerization degree increases layer buckling, and the interruption from the sodium cyanamate moiety also leads to distortion of the conjugated heptazine structure. As a result, PCN-NaCA-*n* samples show increased absorbance not only at  $\pi - \pi^*$  transition but also at  $n - \pi^*$  transition at 450 – 500 nm.

In the Tauc plots from Kubelka-Munk function transformation, the optical band gap is determined to be 2.75 eV for PCN (Fig. 4b). Introduction of the sodium cyanamate moiety into the carbon nitride framework narrows the band gap, e.g. 2.73, 2.69, and 2.63 eV for PCN-NaCA-1, PCN-NaCA-2, and PCN-NaCA-3, respectively. PCN and PCN-NaCA-2 shows the same valence band potential of 1.57 V (vs. RHE) as determined by XPS valence band spectra (Fig. 4c). The conduction band potentials of PCN and PCN-NaCA-2 are accordingly determined to be - 1.18 and - 1.12 V (vs. RHE), demonstrating that  $2e^-$  ORR by conduction band electrons is thermodynamically feasible (Fig. 4d). The enhanced photon absorption is a primary prerequisite for the high activity of  $H_2O_2$  production, as this step provides the initial driving force for the whole solar energy conversion process.

Upon photon absorption, the excited photocatalyst will either relax to the ground state *via* photoluminescence (PL) or transit to non-emissive state through charge trapping wherein some of the trapped charges will participate in the expected surface chemical reaction steps. Steady-state and transient PL spectroscopy is thus employed as an indirect method for analyzing the situation of the trapped charges. As shown in Fig. 4e, PCN shows strong PL emission peak at 488 nm, while the emission intensity of PCN-NaCA-2 is significantly attenuated. Moreover, considering the stronger photon absorption of PCN-NaCA-2 than PCN, much larger proportion of the excited states should transit to the non-emissive states on PCN-NaCA-2 than PCN at this stage.<sup>55</sup> It is also interesting to note a blue shift of 18 nm for PCN-NaCA-2 as compared to that of PCN, which is attributed to the quantum confinement caused by the decreased thickness of the layer stacking.<sup>53,-</sup>

To further understand the variation of the electronic structure of the conjugated system with sodium cyanamate moiety, the decay kinetics of the emissive state is thereafter analyzed by time resolved photoluminescence spectroscopy. As shown in Fig. 4f, PCN-NaCA-2 shows faster PL decay kinetics than that of PCN, showing average lifetime of 3.46 and 8.27 ns for PCN-NaCA-2 and PCN, respectively (Table S2). The shorter lifetime and weaker PL emission intensity of PCN-NaCA-2 compared to PCN indicates the fast quenching of luminescence. This might be attributed to the fact that charges separation is significantly enhanced by extended  $\pi$ -conjugated systems and delocalization of the  $\pi$ -electrons due to improved polymerization degree.

We then focus on the status of the non-emissive trapped electrons and their interaction with the surface adsorbed dioxygen on PCN and PCN-NaCA-2. Femtosecond transient absorption spectroscopy (fs-TAS) was thus employed to quantitatively monitor the population of the trapped electrons and their decay kinetics. The main objective in this stage is to elucidate the unknown interaction between the adsorbed

dioxygen and the photo-induced electrons. All the fs-TAS characterization was thus conducted in the presence of glycerol as the electron/proton donor.

Under vacuum condition, after excitation by laser pulse with photon fluence of  $79.6 \mu\text{J}/\text{cm}^2$ , PCN-NaCA-2 presents characteristic broad absorption peak at 640 nm, which is identified as trapped electrons (Figs. 4a, 4b, and S6). Fig. 5c shows the decay kinetics profiles of the photo-induced electrons with various photon fluence, and the initial absorption intensity depends on the photon fluence, demonstrating the direct impact of the photon fluence on the population of the trapped photo-induced electrons. With the increase of the photon fluence from  $35.8 \mu\text{J}/\text{cm}^2$  to  $79.6 \mu\text{J}/\text{cm}^2$ , the half-life time ( $t_{0.5}$ ) of the trapped electrons decreases from 45 to 25 ps (Fig. 6). However, further increasing the excitation energy to  $278.7 \mu\text{J}/\text{cm}^2$  slightly changed  $t_{0.5}$  (24 ps), which indicates that the effect of excitation fluence on the electron life time is saturated under high photon fluence. In the presence of glycerol as the electron donor under vacuum, the photo-induced electrons accumulate and create electric field which accelerates the decay kinetics of the photo-induced electrons.<sup>66</sup>

Femtosecond-TAS was also measured in pure  $\text{O}_2$  atmosphere for monitoring the impact of the surface adsorbed dioxygen on the trapped electrons. Since dioxygen is an efficient electron acceptor, the accumulation of trapped electrons (i.e., transient absorption intensity) is expected to be lower under oxygen atmosphere than under vacuum. Contrary to the expectation, the presence of dioxygen markedly enhances the transient absorption intensity and modulates the shape of the absorption peak at 660 nm as compared with that in vacuum condition under the same photon fluence conditions (Figs. 4d, 4e, 4f, and S6). The intense absorption peak indicates higher population of trapped electrons, and the well-defined shape of the absorption peak indicates that the distribution of the electron trapping species/sites may be different from those in vacuum.

Upon the fs-laser excitation, the initial transient absorption peak increases linearly with the excitation energy intensity, and the slope is similar between the vacuum and  $\text{O}_2$  atmosphere conditions (Fig. 6). The fact that the transient absorption of trapped electrons is consistently higher in the presence of  $\text{O}_2$  than in vacuum regardless of the excitation energy intensity implies that more trapped electrons are induced in the presence of surface adsorbed  $\text{O}_2$ . In addition, it should be also noted that the half-life time (in 10–100 ps range) of the trapped electrons in oxygen atmosphere is longer than that in vacuum. This indicates that the interaction between surface adsorbed dioxygen and the photo-induced electrons starts at a very early stage of electrons trapping step (in ps to ns time scale), which is opposite to the fact that the interfacial electron transfer from the irradiated semiconductor to  $\text{O}_2$  occurs much later in  $\mu\text{s}$  to ms time scale.<sup>66</sup> It seems that the dioxygen adsorption induces the formation of electron trapping sites on the surface of PCN-NaCA-2 in the ps-ns time range and the transfer of trapped electrons to  $\text{O}_2$  occurs at a much later stage ( $\mu\text{s}$ -ms time region). On the other hand, pure PCN exhibited no absorption peak of trapped electrons in fs-TAS, and only a bleaching signal around 480–540 nm is observed (Figure S7) in both  $\text{O}_2$  atmosphere and vacuum conditions. There is obvious difference in the shape and position of the bleach signal, i.e., sharp peak at 494 nm under vacuum and broad peak at 510 nm in  $\text{O}_2$  conditions. The

decay kinetics of the bleach signal for PCN is, however, similar in vacuum and dioxygen atmosphere (Figure S8). The clear effects of O<sub>2</sub> on the TAS profiles in PCN-NaCA-2 and PCN systems demonstrate that the dioxygen adsorption directly influences the electronic structures of the polymeric photocatalysts. The comparison of fs-TAS between PCN-NaCA-2 and PCN confirms that the photo-induced electron accumulation is uniquely observed on PCN-NaCA-2, not on PCN; and surface dioxygen adsorption further increases the population and prolongs the life time of the trapped electrons on PCN-NaCA-2. These characteristics of PCN-NaCA-2 should make it suitable for producing H<sub>2</sub>O<sub>2</sub> through surface catalytic ORR process.

The trapped electrons and holes, after charges separation, then transport to the surface of the photocatalyst, and initiate the interfacial electron transfer process for chemical reactions. Surface photovoltage (SPV) spectroscopy is a useful tool for analyzing the photo-induced charge transfer processes. SPV spectroscopy records the change of the photovoltage as a function of the wavelength of the excitation photon. The intensity of SPV signal is proportional to the amount of surface trapped charges; and the sign (positive or negative) of photovoltage is correlated to the direction of the charge transport. As shown in Fig. 7a, PCN presents very weak positive photovoltage peaks of 0.00149 mV at 324 nm and 0.00120 mV at 365 nm, indicating that the positive charges accumulate at the surface area nearby the top electrode under irradiation.<sup>68-72</sup> However, PCN-NaCA-2 presents an outstanding negative SPV signal of -0.0510 mV at 364 nm, demonstrating that large amount of electrons accumulated on the surface upon irradiation.

The charges transport kinetics is investigated by transient photovoltage (TPV) characterization. As shown in Fig. 7b, for both PCN and PCN-NaCA-2, the photovoltage signal appears with 0.8 μs delay, which should be ascribed to the diffusion of the charges in the nanoparticle layer. It is noteworthy that, for PCN-NaCA-2, the sign of photovoltage reverses during charge accumulation. From 0.8 μs to 1.4 μs, there is a positive photovoltage observed. After 1.4 μs, photo-induced electrons accumulate on the surface, resulting in a remarkable photovoltage of -1.66 mV at 11.6 μs. The negative photovoltage signal persists for 2.45 ms before it decays to zero, while the surface accumulated charges survive for a much shorter period of 0.60 ms on PCN.

Electrochemical impedance spectroscopic analysis was conducted to further analysed the type of conductivity of PCN-NaCA-2 (Figure S9). In the Mott-Schottky plots, the negative and positive slopes, respectively, correspond to p-type and n-type conductivities. This indicates the co-existence of the both p-type and n-type domains within PCN-NaCA-2. The p-type conductivity might be attributed to the strong electron withdrawing property of the cyanamino-moiety in the framework. The above analysis reveals that the PCN-NaCA-2 with both p-type and n-type domains, yields much larger number of trapped electrons on the surface region as compared to the n-type PCN, which makes PCN-NaCA-2 more suitable for ORR than PCN.

The final step in the photo-production of H<sub>2</sub>O<sub>2</sub> is the interfacial transfer of the trapped electrons to the adsorbed O<sub>2</sub>. The interaction between the catalysts surface and the dioxygen molecules is thus studied

by the temperature programmed oxygen desorption ( $O_2$ -TPD) wherein the area of the desorption peak indicates the amount of dioxygen adsorbed per unit catalyst mass and the desorption temperature estimates the surface binding energy of dioxygen. As shown in Fig. 7c, PCN-NaCA-2 exhibits significantly higher  $O_2$  adsorption capacity (by mass), which is around 3 times larger than that of the pristine PCN. Moreover, PCN-NaCA-2 has a much lower BET surface area than that of PCN, i.e.,  $11.9 \text{ m}^2/\text{g}$  for PCN-NaCA-2 versus  $83.2 \text{ m}^2/\text{g}$  for PCN. This implies that the density of the surface adsorbed dioxygen on PCN-NaCA-2 is around 20 times larger than that on PCN. More importantly, it is noted that PCN-NaCA-2 has much higher surface binding affinity for  $O_2$ , as the  $O_2$  desorption peak on PCN-NaCA-2 appears at  $160 \text{ }^\circ\text{C}$ , much higher than that of PCN at  $104 \text{ }^\circ\text{C}$ . The stronger surface binding affinity for  $O_2$  as well as the high density of adsorbed  $O_2$  should contribute synergically to the highly enhanced ORR activity.

Finally, for an efficient  $H_2O_2$  production, the selectivity towards  $2e^-$  ORR is of critical importance. The performance of  $2e^-$  ORR to  $H_2O_2$  is thus evaluated by analyzing its electrochemical selectivity on a rotating ring disc electrode (RRDE) wherein the disc current comes from the dioxygen reduction reactions (including  $1e^-$ ,  $2e^-$ , and  $4e^-$  transfer pathways) and the ring current comes from the  $2e^-$  oxidation of  $H_2O_2$  produced from the disc. Figure 7d shows linear sweep voltammetry (LSV) curves with PCN-NaCA-2 as the active material in oxygen-saturated KOH electrolyte. It should be particularly noted that the disc current density and ring current density reach  $-0.5677$  and  $0.7507 \text{ mA}/\text{cm}^2$ , respectively (at the applied voltage of  $-0.425 \text{ V}$  (vs. Ag/AgCl) and rotation speed of  $100 \text{ rpm}$ ), which yields a remarkable  $H_2O_2$  selectivity of  $99.8\%$ . Under otherwise the same test condition, PCN exhibits much lower disc current density and ring current density of  $-0.3838$  and  $0.1547 \text{ mA}/\text{cm}^2$ , respectively, which gives a poor  $H_2O_2$  selectivity of  $46.6\%$  (Fig. 7e). The RRDE measurements thus demonstrate that PCN-NaCA-2 exhibits superior activity and selectivity for  $2e^-$  ORR as compared to PCN. This indicates that the formation of sodium cyanamate moiety on PCN-NaCA-2 creates surface active sites which are particularly favorable for  $2e^-$  ORR pathway.

For further understanding the fundamental mechanism of the above-mentioned superior surface-catalytic  $2e^-$  ORR performance, we carried out theoretical simulation based on proposed  $2e^-$  ORR steps in alkaline solution. Figures 7a and 7b show, respectively, the optimized configurations of the surface dioxygen adsorption on PCN and PCN-NaCA-2. The adsorption of dioxygen on PCN is very weak, presenting an adsorption energy of  $-0.017 \text{ eV}$  (Fig. 8e), which is mainly Van der Waals interaction. On the other hand, PCN-NaCA-2 exhibits much higher adsorption energy of  $-0.446 \text{ eV}$  (Fig. 8e), which explains why the strong surface dioxygen affinity was observed in the  $O_2$ -TPD characterization. This high adsorption energy may result from the interaction between surface adsorbed dioxygen with conjugated  $\pi$ -electrons as well as the sodium cation. The free energy of the intermediate  $*OOH$  on PCN-NaCA-2 drops further to  $-0.784 \text{ eV}$ , which is much lower than that on PCN (Figs. 7c, 7d, and 7e). From the above analysis, it is evident that  $2e^-$  ORR pathway is energetically more favorable on PCN-NaCA-2 surface than on PCN surface.

## Discussion

In the solar-driven selective  $2e^-$  ORR using the biomass-derived glycerol as the electron/proton donor, the carbon nitride framework with cyanamate sodium salt moiety exhibits superior photoactivity for  $H_2O_2$  production, which is 24.6 times of that on PCN in a continuous flow photo-reaction. The critical factors and steps in the overall photoconversion process, which include the band energy levels, photon absorption, charge recombination/separation/trapping, dioxygen adsorption, and interfacial electron transfer, were investigated systematically by a series of steady-state and transient spectroscopic techniques. The formation of the sodium cyanamate moiety on the PCN framework significantly influences the above-mentioned critical factors and steps. In particular, it should be noted that surface adsorbed dioxygen molecules on PCN-NaCA-2 unexpectedly enhance not only the population of trapped electrons but also their lifetime in the ps-ns time region, whereas the interfacial transfer of trapped electrons to  $O_2$  to form  $H_2O_2$  should take place in a much later stage. This indicates that creating unique surface sites with strong affinity for trapping both  $O_2$  and electrons should be an essential component in designing efficient photocatalysts for solar-driven  $H_2O_2$  production. Introducing the cyanamate moiety to the PCN framework has the following multiple effects: (1) enhancing photon absorption, (2) creating coexistence of p-type and n-type domains with retarded radiative charge recombination and improved electrons accumulation in the surface region, (3) enhancing surface adsorption of dioxygen molecules, and (4) favoring highly selective  $2e^-$  ORR, all of which synergistically contributes to the extraordinary performance of solar-driven  $H_2O_2$  production.

## Declarations

### Acknowledgements

Financial supports from National Natural Science Foundation of China (NOs. 21976041, 51538013, 51838005) and Brain Pool Program through the National Research Foundation of Korea (NRF) (2018H1D3A2065393) are acknowledged. We are grateful to Prof. Markus Antonietti, Prof. Wanhong Ma, Prof. Tengfeng Xie, Prof. Guigang Zhang, and Dr. Wenxing Yang for fruitful discussions.

### Author contributions

Y.Z. and W.C. conceived the project and designed the experiments; Y.Z., L.N., S.C. and W.C. conducted the experiments and data analysis; Y.Z., S.C., and W.C. wrote the original draft; Y.Z., C.H. and W.C. supervise the project. All authors commented on the final manuscript.

### Declaration of interests

The authors declare no competing interests.

## References

- 1 . Schultz, D. M. & Yoon, T. P. Solar synthesis: prospects in visible light photocatalysis. *Science* 343, 1239176 (2014).
- 2 . Fukuzumi, S., Lee, Y.-M. & Nam, W. Solar-driven production of hydrogen peroxide from water and dioxygen. *Chem. Eur. J.* 24, 5016-5031 (2017).
- 3 . Yamada, Y., Yoneda, M. & Fukuzumi, S. High and robust performance of H<sub>2</sub>O<sub>2</sub> fuel cells in the presence of scandium ion. *Energy Environ. Sci.* 8, 1698-1701 (2015).
- 4 . Mase, K., Yoneda, M., Yamada, Y. & Fukuzumi, S. Seawater usable for production and consumption of hydrogen peroxide as a solar fuel. *Nat. Commun.* 7, 11470 (2016).
- 5 . Myers, R.L. *The 100 most important chemical compounds: a reference guide*, First edition (Greenwood Publishing Group), pp. 352 (2007).
- 6 . Edwards, J. K. et al. Switching off hydrogen peroxide hydrogenation in the direct synthesis process. *Science* 323, 1037-1041 (2009).
- 7 . Edwards, J. K. et al. Direct Synthesis of H<sub>2</sub>O<sub>2</sub> from H<sub>2</sub> and O<sub>2</sub> over Gold, Palladium, and Gold-Palladium Catalysts Supported on Acid-Pretreated TiO<sub>2</sub>. *Angew. Chem. Int. Ed.* 48, 8512-8515 (2009).
- 8 . Liu, Q., Bauer, J. C., Schaak, R. E. & Lunsford, J. H. Supported palladium nanoparticles: an efficient catalyst for the direct formation of H<sub>2</sub>O<sub>2</sub> from H<sub>2</sub> and O<sub>2</sub>. *Angew. Chem. Int. Ed.* 47, 6221-6224 (2008).
- 9 . Xia, C., Xia, Y., Zhu, P., Fan, L. & Wang, H. Direct electrosynthesis of pure aqueous H<sub>2</sub>O<sub>2</sub> solutions up to 20% by weight using a solid electrolyte. *Science* 366, 226-231 (2019).
- 10 . Smith, W. A., Sharp, I. D., Strandwitz, N. C. & Bisquert, J. Interfacial band-edge energetics for solar fuels production. *Energy Environ. Sci.* 8, 2851-2862 (2015).
- 11 . Hou, H., Zeng, X. & Zhang, X. Production of hydrogen peroxide through photocatalytic processes: a critical review of recent advances. *Angew. Chem. Int. Ed.* doi:10.1002/anie.201911609 (2019).
- 12 . Krivtsov, I. et al. Water-Soluble Polymeric Carbon Nitride Colloidal Nanoparticles for Highly Selective Quasi-Homogeneous Photocatalysis. *Angew. Chem. Int. Ed.* 59, 487-495 (2020).
- 13 . Jeon, T. H., Kim, H., Kim, H.-i. & Choi, W. Highly durable photoelectrochemical H<sub>2</sub>O<sub>2</sub> production via dual photoanode and cathode processes under solar simulating and external bias-free conditions. *Energy Environ. Sci.* 13, 1730-1742 (2020).
- 14 . Fan, W. et al. Efficient hydrogen peroxide synthesis by metal-free polyterthiophene via photoelectrocatalytic dioxygen reduction. *Energy Environ. Sci.* 13, 238-245 (2020).

- 15 . Moon, G.-h. et al. Eco-Friendly Photochemical production of H<sub>2</sub>O<sub>2</sub> through O<sub>2</sub> reduction over carbon nitride frameworks incorporated with multiple heteroelements. *ACS Catal.* 7, 2886-2895 (2017).
- 16 . Zhang, P. et al. Modified carbon nitride nanozyme as bifunctional glucose oxidase-peroxidase for metal-free bioinspired cascade photocatalysis. *Nat. Commun.* 10, 940 (2019).
- 17 . Wei, Z. et al. Efficient visible-light-driven selective oxygen reduction to hydrogen peroxide by oxygen-enriched graphitic carbon nitride polymers. *Energy Environ. Sci.* 11, 2581-2589 (2018).
- 18 . Wang, X. et al. A metal-free polymeric photocatalyst for hydrogen production from water under visible light. *Nat. Mater.* 8, 76-80 (2009).
- 19 . Cao, S., Low, J., Yu, J. & Jaroniec, M. Polymeric photocatalysts based on graphitic carbon nitride. *Adv. Mater.* 27, 2150-2176 (2015).
- 20 . Zhang, G., Lan, Z.-A. & Wang, X. Conjugated polymers: catalysts for photocatalytic hydrogen evolution. *Angew. Chem. Int. Ed.* 55, 15712-15727 (2016).
- 21 . Ghosh, I. et al. Organic semiconductor photocatalyst can bifunctionalize arenes and heteroarenes. *Science* 365, 360-366 (2019).
- 22 . Zhao, Y. & Antonietti, M. Visible-light-irradiated graphitic carbon nitride photocatalyzed Diels-Alder reactions with dioxygen as sustainable mediator for photoinduced electrons. *Angew. Chem. Int. Ed.* 56, 9336-9340 (2017).
- 23 . Zhao, Y. et al. The Surface-structure sensitivity of dioxygen activation in the anatase-photocatalyzed oxidation reaction. *Angew. Chem. Int. Ed.* 51, 3188-3192 (2012).
- 24 . Li, L. et al. Photocatalytic cyanation of carbon nitride scaffolds: tuning band structure and enhancing the performance in green light driven C-S bond formation. *Appl. Catal. B-Environ.* 229, 249-253 (2018).
- 25 . Zhang, G. et al. Electron Deficient Monomers that Optimize Nucleation and Enhance the Photocatalytic Redox Activity of Carbon Nitrides. *Angew. Chem. Int. Ed.* 58, 14950-14954 (2019).
- 26 . Lau, V. W.-h. et al. Rational design of carbon nitride photocatalysts by identification of cyanamide defects as catalytically relevant sites. *Nat. Commun.* 7, 12165 (2016).
- 27 . Lau, V. W.-h. et al. Urea-modified carbon nitrides: enhancing photocatalytic hydrogen evolution by rational defect engineering. *Adv. Energy Mater.* 7, 1602251 (2017).
- 28 . Fujishima, A., Zhang, X. & Tryk, D. A. TiO<sub>2</sub> photocatalysis and related surface phenomena. *Surf. Sci. Rep.* 63, 515-582 (2008).

- 29 . Godin, R., Wang, Y., Zwiijnenburg, M. A., Tang, J. & Durrant, J. R. Time-resolved spectroscopic investigation of charge trapping in carbon nitrides photocatalysts for hydrogen generation. *J. Am. Chem. Soc.* 139, 5216-5224 (2017).
- 30 . Ong, W.-J., Tan, L.-L., Ng, Y. H., Yong, S.-T. & Chai, S.-P. Graphitic carbon nitride (g-C<sub>3</sub>N<sub>4</sub>)-based photocatalysts for artificial photosynthesis and environmental remediation: are we a step closer to achieving sustainability? *Chem. Rev.* 116, 7159-7329 (2016).
- 31 . Dontsova, D. et al. Triazoles: A new class of precursors for the synthesis of negatively charged carbon nitride derivatives. *Chem. Mater.* 27, 5170-5179 (2015).
- 32 . Kasap, H. et al. Solar-driven reduction of aqueous protons coupled to selective alcohol oxidation with a carbon nitride–molecular ni catalyst system. *J. Am. Chem. Soc.* 138, 9183-9192 (2016).
- 33 . Shalom, M., Inal, S., Fettkenhauer, C., Neher, D. & Antonietti, M. Improving carbon nitride photocatalysis by supramolecular preorganization of monomers. *J. Am. Chem. Soc.* 135, 7118-7121 (2013).
- 34 . Lin, L., Yu, Z. & Wang, X. Crystalline carbon nitride semiconductors for photocatalytic water splitting. *Angew. Chem. Int. Ed.* 58, 6164-6175 (2019).
- 35 . Zhang, G. et al. Tailoring the grain boundary chemistry of polymeric carbon nitride for enhanced solar hydrogen production and CO<sub>2</sub> reduction. *Angew. Chem. Int. Ed.* 58, 3433-3437 (2019).
- 36 . Bojdys, M. J., Müller, J.-O., Antonietti, M. & Thomas, A. Ionothermal synthesis of crystalline, condensed, graphitic carbon nitride. *Chem. Eur. J.* 14, 8177-8182 (2008).
- 37 . Liu, X., Fechler, N. & Antonietti, M. Salt melt synthesis of ceramics, semiconductors and carbon nanostructures. *Chem. Soc. Rev.* 42, 8237-8265 (2013).
- 38 . Shiraishi, Y. et al. Resorcinol–formaldehyde resins as metal-free semiconductor photocatalysts for solar-to-hydrogen peroxide energy conversion. *Nat. Mater.* 18, 985-993 (2019).
- 39 . Shiraishi, Y. et al. Sunlight-Driven Hydrogen Peroxide Production from Water and Molecular Oxygen by Metal-Free Photocatalysts. *Angew. Chem. Int. Ed.* 53, 13454-13459 (2014).
- 40 . Shiraishi, Y. et al. Effects of Surface Defects on Photocatalytic H<sub>2</sub>O<sub>2</sub> Production by Mesoporous Graphitic Carbon Nitride under Visible Light Irradiation. *ACS Catal.* 5, 3058-3066 (2015).
- 41 . Teng, Z. et al. Edge-functionalized g-C<sub>3</sub>N<sub>4</sub> nanosheets as a highly efficient metal-free photocatalyst for safe drinking water. *Chem* 5, 664-680 (2019).
- 42 . Govindjee W. J. *Concepts in photobiology: photosynthesis and photomorphogenesis* (Kluwer Academic Publishers), pp. 11-51 (1999).

- 43 . Meher, L. C., Vidya Sagar, D. & Naik, S. N. Technical aspects of biodiesel production by transesterification-a review. *Renewable Sustainable Energy Rev.* 10, 248-268 (2006).
- 44 . Zhou, C.-H., Beltramini, J. N., Fan, Y.-X. & Lu, G. Q. Chemoselective catalytic conversion of glycerol as a biorenewable source to valuable commodity chemicals. *Chem. Soc. Rev.* 37, 527-549 (2008).
- 45 . Verma, S., Lu, S. & Kenis, P. J. A. Co-electrolysis of CO<sub>2</sub> and glycerol as a pathway to carbon chemicals with improved techno-economics due to low electricity consumption. *Nat. Energy* 4, 466-474 (2019).
- 46 . Wang, X. et al. Polymer semiconductors for artificial photosynthesis: hydrogen evolution by mesoporous graphitic carbon nitride with visible light. *J. Am. Chem. Soc.* 131, 1680-1681 (2009).
- 47 . Pieber, B., Shalom, M., Antonietti, M., Seeberger, P. H. & Gilmore, K. Continuous heterogeneous photocatalysis in serial micro-batch reactors. *Angew. Chem. Int. Ed.* 57, 9976-9979 (2018).
- 48 . Zhao, Y. & Antonietti, M. Visible-light-driven conversion of alcohols into iodide derivatives with iodoform. *ChemPhotoChem* 2, 720-724 (2018).
- 49 . Geyer, K., Codée, J. D. C. & Seeberger, P. H. Microreactors as tools for synthetic chemists—the chemists' round-bottomed flask of the 21st century? *Chem. Eur. J.* 12, 8434-8442 (2006).
- 50 . Laudadio, G. et al. C(sp<sup>3</sup>)-H functionalizations of light hydrocarbons using decatungstate photocatalysis in flow. *Science* 369, 92-96 (2020).
- 51 . Deifallah, M., McMillan, P. F. & Corà, F. Electronic and structural properties of two-dimensional carbon nitride graphenes. *J. Phys. Chem. C* 112, 5447-5453 (2008).
- 52 . Jorge, A. B. et al. H<sub>2</sub> and O<sub>2</sub> evolution from water half-splitting reactions by graphitic carbon nitride materials. *J. Phys. Chem. C* 117, 7178-7185 (2013).
- 53 . Thomas, A. et al. Graphitic carbon nitride materials: variation of structure and morphology and their use as metal-free catalysts. *J. Mater. Chem.* 18, 4893-4908 (2008).
- 54 . Zhang, H. & Yu, A. Photophysics and photocatalysis of carbon nitride synthesized at different temperatures. *J. Phys. Chem. C* 118, 11628-11635 (2014).
- 55 . Khan, M. A., Maity, P., Al-Oufi, M., Al-Howaish, I. K. & Idriss, H. Electron transfer of the metal/semiconductor system in photocatalysis. *J. Phys. Chem. C* 122, 16779-16787 (2018).
- 56 . Tyborski, T. et al. Crystal structure of polymeric carbon nitride and the determination of its process-temperature-induced modifications. *J. Phys.: Condens. Matter* 25, 395402 (2013).

- 57 . Yu, H. et al. Alkali-assisted synthesis of nitrogen deficient graphitic carbon nitride with tunable band structures for efficient visible-light-driven hydrogen evolution. *Adv. Mater.* 29, 1605148 (2017).
- 58 . Corp, K. L. & Schlenker, C. W. Ultrafast spectroscopy reveals electron-transfer cascade that improves hydrogen evolution with carbon nitride photocatalysts. *J. Am. Chem. Soc.* 139, 7904-7912 (2017).
- 59 . Merschjann, C. et al. Photophysics of polymeric carbon nitride: An optical quasimonomer. *Phys. Rev. B* 87, 205204 (2013).
- 60 Alivisatos, A. P. Semiconductor Clusters, Nanocrystals, and Quantum Dots. *Science* 271, 933-937 (1996).
- 61 Niu, P, Zhang, L., Liu, G. & Cheng, H.-M. Graphene-like carbon nitride nanosheets for improved photocatalytic activities. *Adv. Funct. Mater.* 22, 4763-4770 (2012).
- 62 Zhang, X. et al. Enhanced photoresponsive ultrathin graphitic-phase C<sub>3</sub>N<sub>4</sub> nanosheets for bioimaging. *J. Am. Chem. Soc.* 135, 18-21 (2013).
- 63 Ou, H., Yang, P., Lin, L., Anpo, M. & Wang, X. Carbon nitride aerogels for the photoredox conversion of water. *Angew. Chem. Int. Ed.* 56, 10905-10910 (2017).
- 64 . Kumar, P. et al. C<sub>3</sub>N<sub>5</sub>: a low bandgap semiconductor containing an azo-linked carbon nitride framework for photocatalytic, photovoltaic and adsorbent applications. *J. Am. Chem. Soc.* 141, 5415-5436 (2019).
- 65 . Liang, Q., Li, Z., Huang, Z.-H., Kang, F. & Yang, Q.-H. Holey graphitic carbon nitride nanosheets with carbon vacancies for highly improved photocatalytic hydrogen production. *Adv. Funct. Mater.* 25, 6885-6892 (2015).
- 66 . Yang, W. et al. Electron accumulation induces efficiency bottleneck for hydrogen production in carbon nitride photocatalysts. *J. Am. Chem. Soc.* 141, 11219-11229 (2019).
- 67 . Kronik, L. & Shapira, Y. Surface photovoltage phenomena: theory, experiment, and applications. *Surf. Sci. Rep.* 37, 1-206 (1999).
- 68 . Jiang, T. et al. Photoinduced charge transfer in ZnO/Cu<sub>2</sub>O heterostructure films studied by surface photovoltage technique. *Phys. Chem. Chem. Phys.* 12, 15476-15481 (2010).
- 69 . Jiang, T., Xie, T., Chen, L., Fu, Z. & Wang, D. Carrier concentration-dependent electron transfer in Cu<sub>2</sub>O/ZnO nanorod arrays and their photocatalytic performance. *Nanoscale* 5, 2938-2944 (2013).
- 70 . Gross, D. et al. Charge Separation in Type II Tunneling Multilayered Structures of CdTe and CdSe Nanocrystals Directly Proven by Surface Photovoltage Spectroscopy. *J. Am. Chem. Soc.* 132, 5981-

5983 (2010).

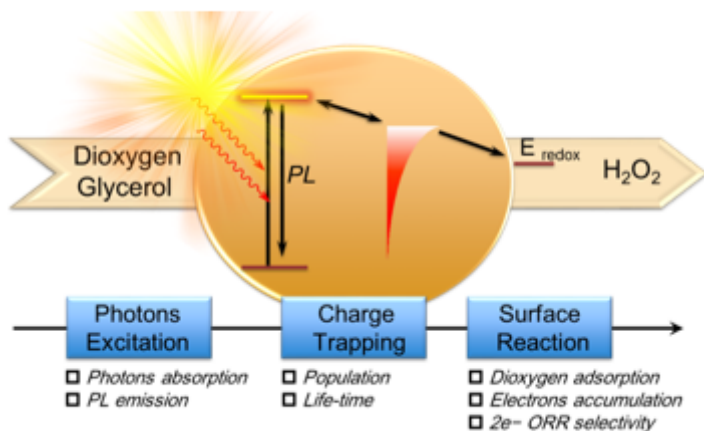
71 . Wei, X. et al. Effect of heterojunction on the behavior of photogenerated charges in Fe<sub>3</sub>O<sub>4</sub>@Fe<sub>2</sub>O<sub>3</sub> nanoparticle photocatalysts. J. Phys. Chem. C 115, 8637-8642 (2011).

72 . Townsend, T. K., Browning, N. D. & Osterloh, F. E. Overall photocatalytic water splitting with NiOx-SrTiO<sub>3</sub> - a revised mechanism. Energy Environ. Sci. 5, 9543-9550 (2012).

73 . Yeh, T.-F., Teng, C.-Y., Chen, S.-J. & Teng, H. Nitrogen-doped graphene oxide quantum dots as photocatalysts for overall water-splitting under visible light illumination. Adv. Mater. 26, 3297-3303 (2014).

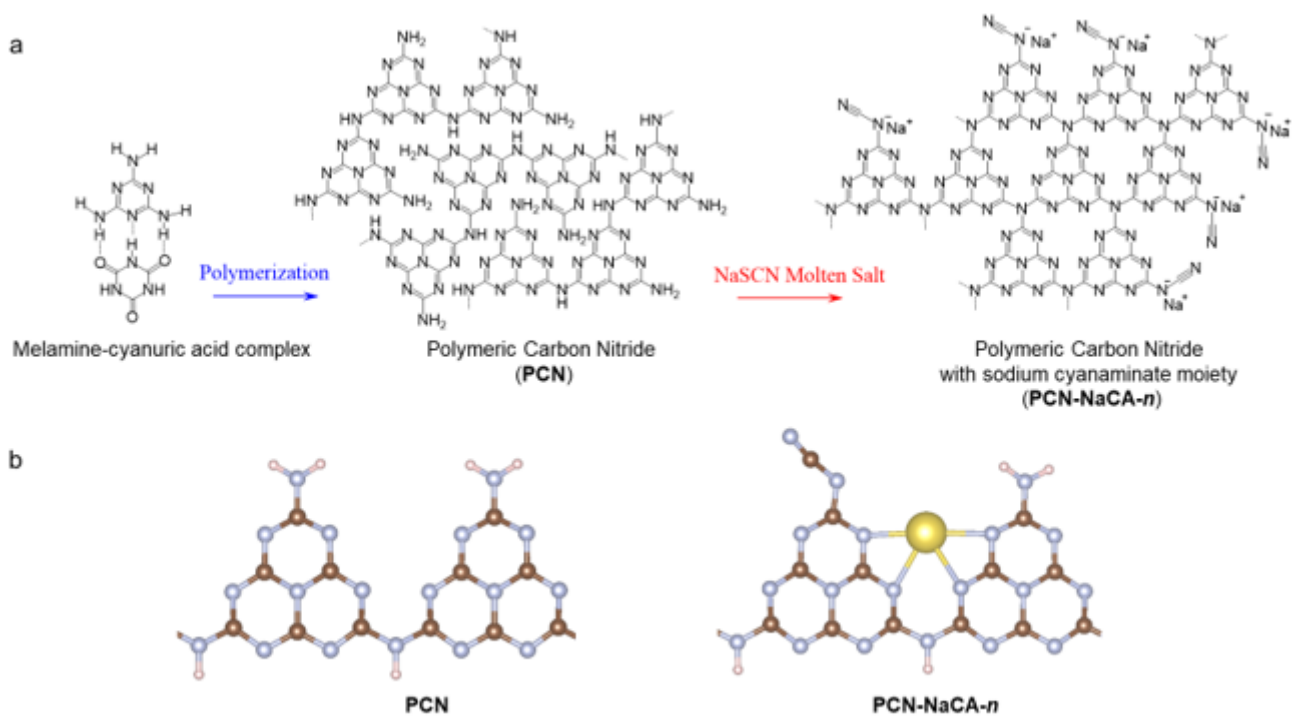
74 . Liu, G. et al. In situ bond modulation of graphitic carbon nitride to construct p-n homojunctions for enhanced photocatalytic hydrogen production. Adv. Funct. Mater. 26, 6822-6829 (2016).

## Figures



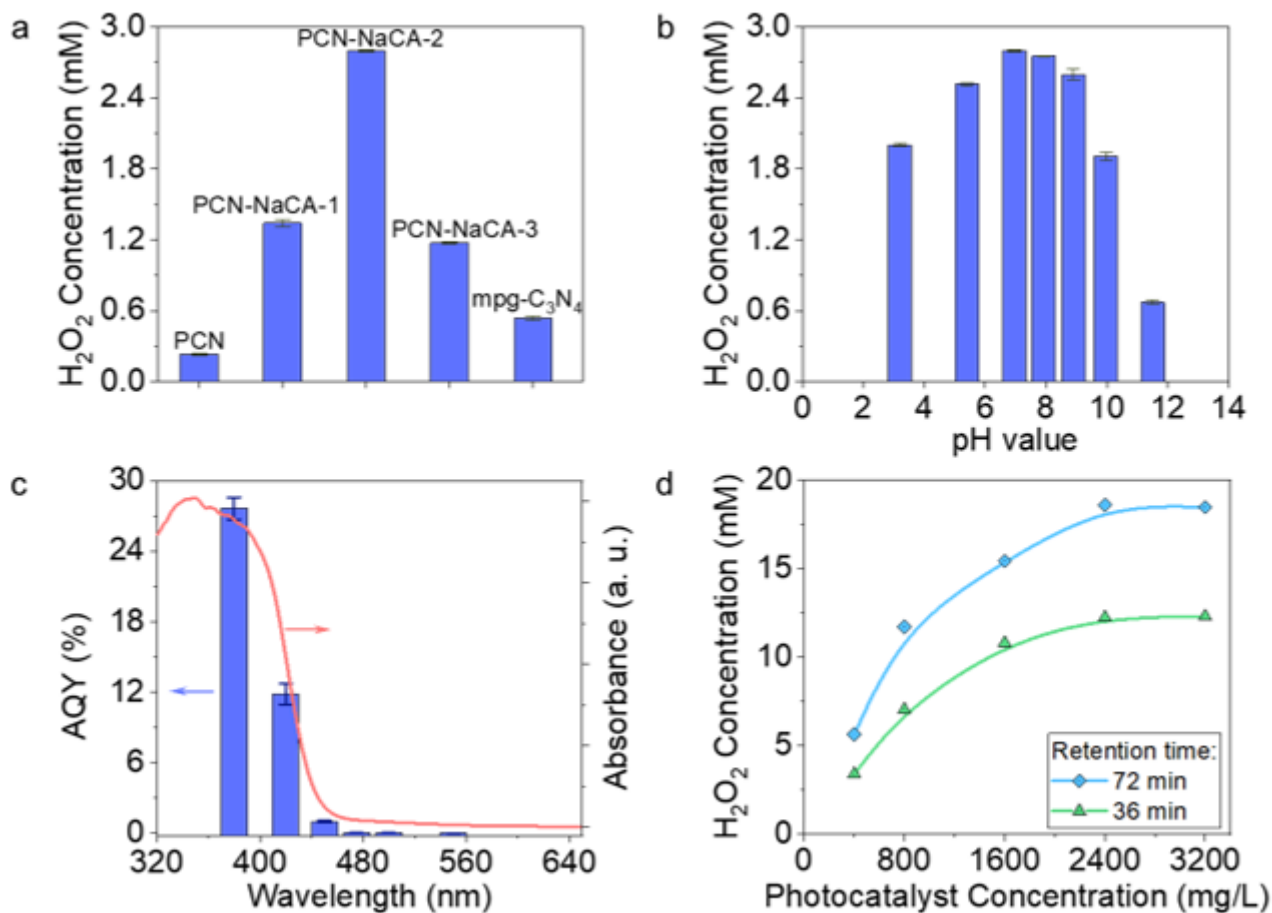
**Figure 1**

Illustration of the sequential mechanisms of the photophysical, photochemical, and surface reaction steps involved in solar-driven H<sub>2</sub>O<sub>2</sub> production process.



**Figure 2**

Synthesis and structure of the photocatalysts. (a) Synthesis of PCN and PCN-NaCA-n. (b) The optimized configurations of PCN and PCN-NaCA-n; two repeating heptazine units out of the infinite linear structure is shown; Atom color code: silver, nitrogen; brown, carbon; pink, hydrogen; yellow, sodium.



**Figure 3**

Solar-driven H<sub>2</sub>O<sub>2</sub> production performance. (a) Comparison of the performances of the photocatalysts in batch reactor with 45 min solar simulator irradiation. (b) The pH-dependence of H<sub>2</sub>O<sub>2</sub> production performance on PCN-NaCA-2. (c) The apparent quantum yield of H<sub>2</sub>O<sub>2</sub> production as a function of wavelength on PCN-NaCA-2. (d) H<sub>2</sub>O<sub>2</sub> production performance as a function of photocatalyst concentration on PCN-NaCA-2 in continuous flow photo-reactor.

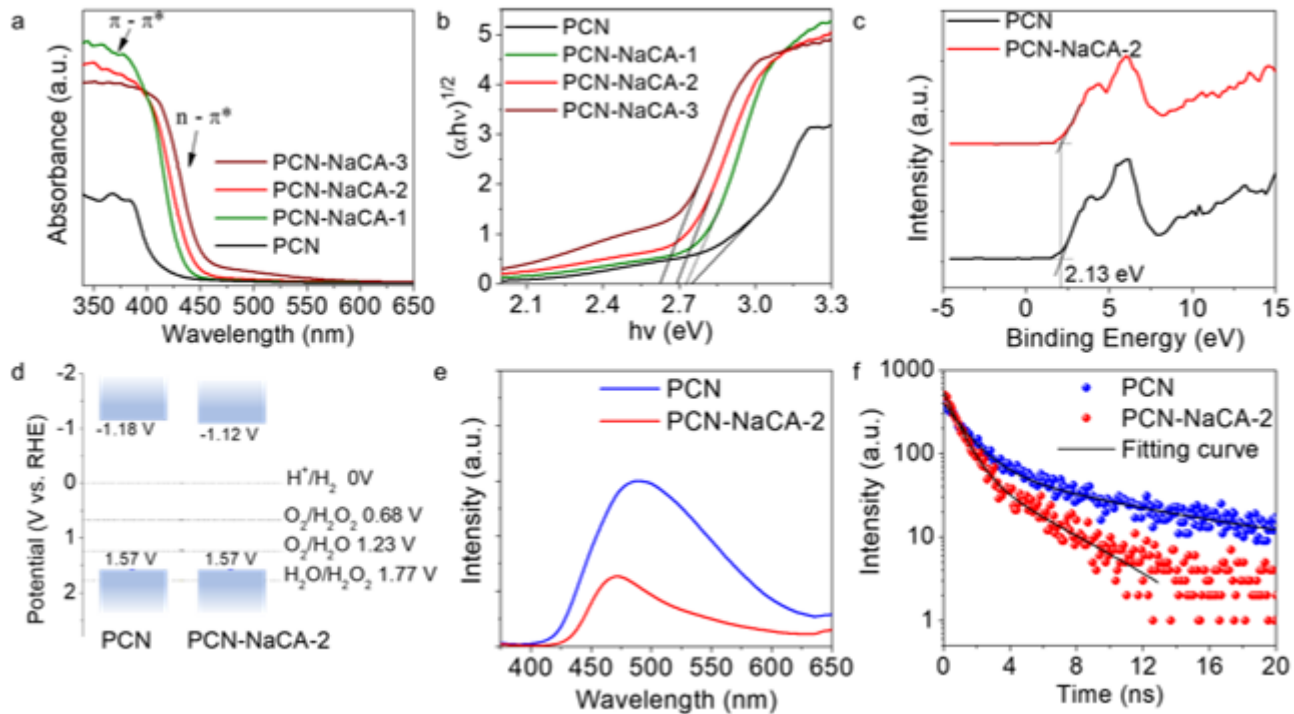


**Figure 4**

Excitation and quenching properties of the photocatalysts. (a) UV-Vis diffuse reflectance spectra. (b) Plots of transformed Kubelka–Munk function versus photon energy. (c) Valence band X-ray photoelectron spectra. (d) Band structure of PCN and PCN-NaCA-2. (e) Steady-state photoluminescence spectra under 355 nm excitation. (f) Time-resolved photoluminescence (TRPL) spectra.

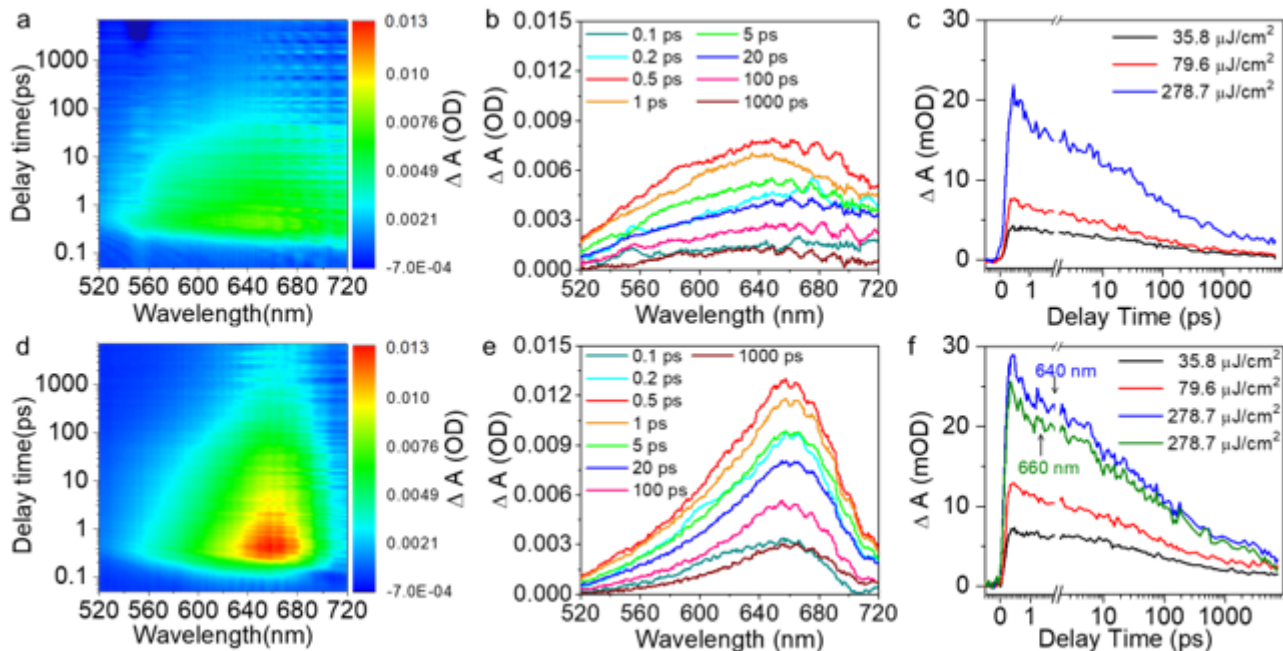


**Figure 5**

Femtosecond transient absorption spectra (fs-TAS) of PCN-NaCA-2. (a and b) fs-TAS upto 7 ns delay times after excitation by 365 nm laser pulse with energy density of  $79.6 \mu\text{J}/\text{cm}^2$  in glycerol aqueous solution (0.38 M) under vacuum. (c) fs-TAS decay kinetics profiles monitored at the wavelength of 640 nm under vacuum with a series of excitation energy densities. (d and e) fs-TAS upto 7 ns delay times after excitation by 365 nm laser pulse with energy density of  $79.6 \mu\text{J}/\text{cm}^2$  in glycerol aqueous solution (0.38 M) in 1 atm.  $\text{O}_2$  atmosphere. (f) fs-TAS decay kinetics profiles monitored at the wavelength of 640 and 660 nm in pure  $\text{O}_2$  atmosphere with a series of excitation energy densities.

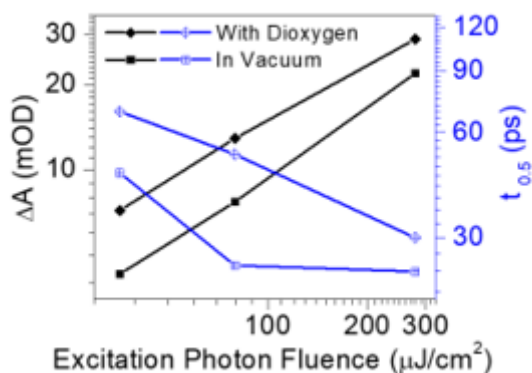


**Figure 6**

The fluence dependence of the initial amplitude (black plots) and the decay half-life (blue plots) of the photo-induced electrons of PCN-NaCA-2 in glycerol aqueous solution in pure oxygen atmosphere and vacuum conditions.

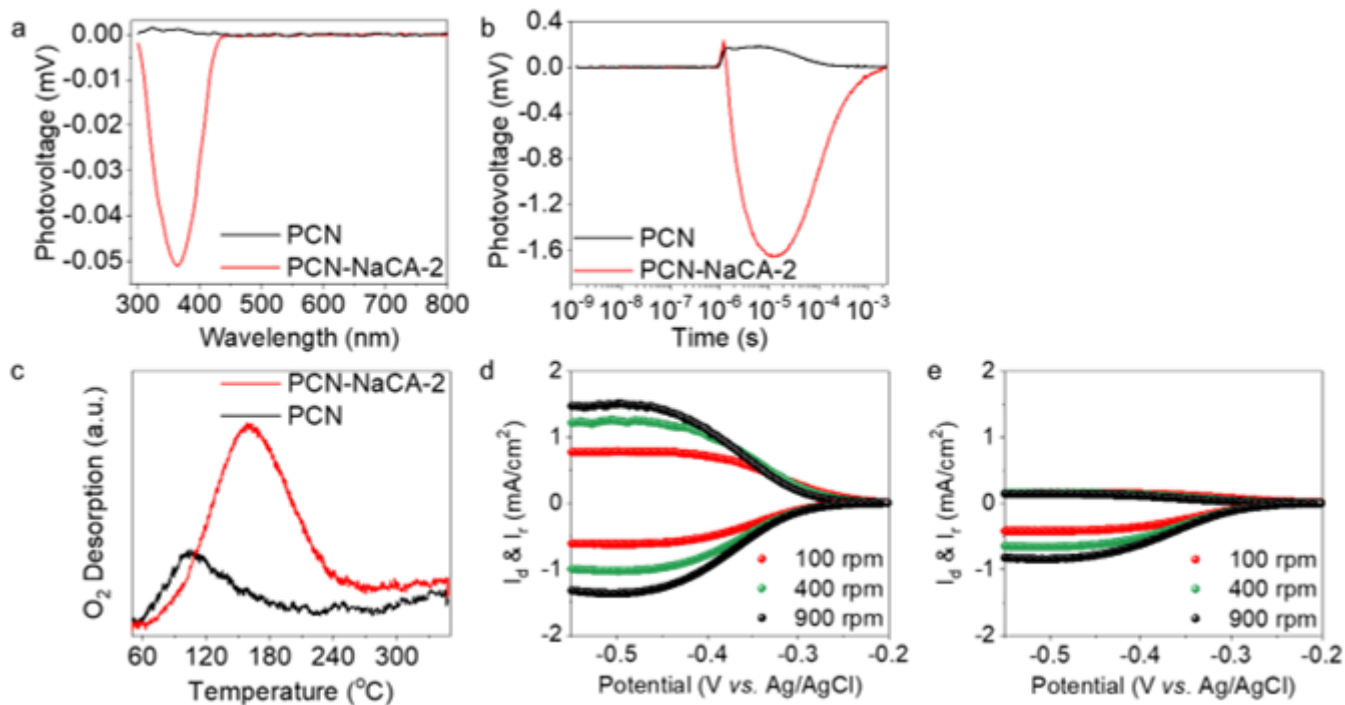


**Figure 7**

Behavior of the charges and dioxygen on the surfaces of PCN and PCN-NaCA-2. (a) Surface photovoltage (SPV) spectra of PCN and PCN-NaCA-2. (b) The transient photovoltage spectra of PCN and PCN-NaCA-2 with 100  $\mu\text{J}$  355 nm pulse excitation. (c) Temperature programmed oxygen desorption (O<sub>2</sub>-TPD) profiles of PCN and PCN-NaCA-2. (d and e) The linear sweep voltammetry (LSV) plots of PCN-NaCA-2 (d) and PCN (e) on rotating ring disk electrode (RRDE);  $I_d$  is the disk current density, and  $I_r$  is the ring current density divided by collection efficiency.

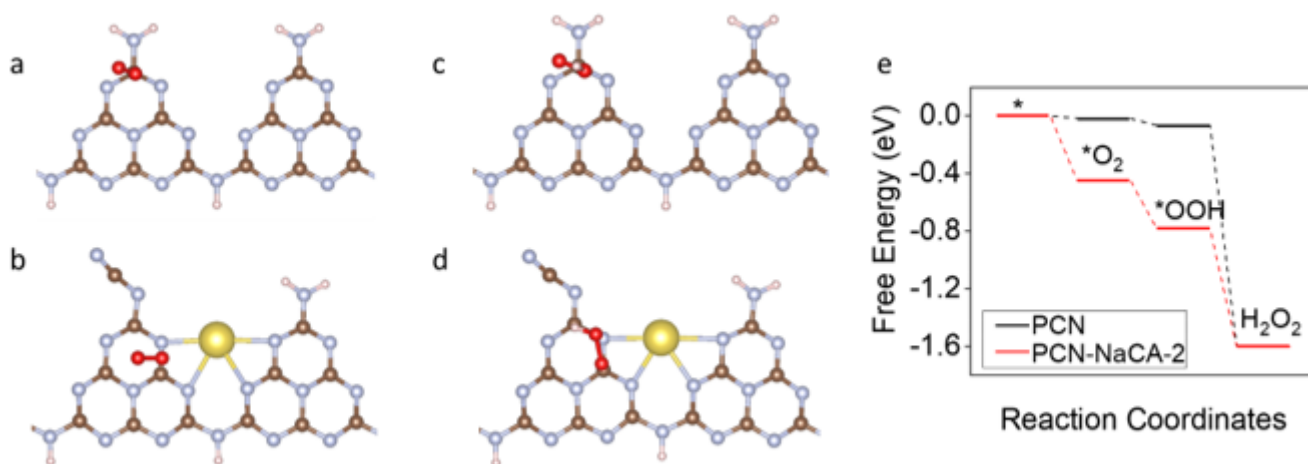


**Figure 8**

Theoretical simulation of the 2e<sup>-</sup> ORR on PCN and PCN-NaCA-2 surface. The optimized configurations of dioxygen adsorption (a and b) and intermediate specie (c and d) on PCN (a and c) and PCN-NaCA-2 (b and d). (e) The free energy variation in 2e<sup>-</sup> ORR pathway; \* represents the surface adsorption sites. Atom color code: silver, nitrogen; brown, carbon; pink, hydrogen; yellow, sodium; red, oxygen.

## Supplementary Files

This is a list of supplementary files associated with this preprint. Click to download.

- [SupplementaryInformation.docx](#)